ROYAL SOCIETY
OF CHEMISTRY

PAPER

View Article Online
View Journal | View Issue

The reverse water gas shift reaction (RWGS) mechanism study on the γ-MoC(100) surface†

Xiaoshu Yao, Zhihong Wei, [ID] * Jingyuan Mei, Xianhui Guo and Xinxin Tian [ID] *

CO_2 conversion and reuse technology are crucial for alleviating environmental stress and promoting carbon cycling. Reverse water gas shift (RWGS) reaction can transform inert CO_2 into active CO. Molybdenum carbide (MoC) has shown good performance in the RWGS reaction, and different crystalline phases exhibit distinct catalytic behaviors. Here, we performed a systematic study on the RWGS reaction mechanism on the hexagonal-phase γ-MoC(100) surface by using density functional theory (DFT). It is found that the redox mechanism, *i.e.* the direct dissociation of CO_2, is the dominant pathway. CO_2 firstly adsorbs on the surface with an adsorption energy of −2.14 eV, and then dissociates into CO* and O* with a barrier of 0.83 eV. Surface O* hydrogenating into OH* has a high barrier of 2.15 eV. OH* further hydrogenating into H_2O* has a barrier of 1.48 eV, and the disproportionation of OH* considerably lowers this value to 0.06 eV. However, the desorption of product CO is particularly challenging due to the large energy demand of 3.06 eV. This characteristic, in turn, provides feasibility and opportunity for CO_2 to serve as a potential alternative carbon source for CO on the γ-MoC(100) surface. In contrast, other Mo-based catalysts such as hexagonal MoP and cubic α-MoC have better RWGS catalytic efficiency.

1 Introduction

Currently, the prevalent view is that greenhouse gases emitted by human activities are the primary cause of global climate change,[1,2] with CO_2 being the most significant component among these gases.[3,4] Consequently, reducing CO_2 emissions and achieving its conversion and reuse are essential methods for addressing the environmental threats posed by its excessive atmospheric concentration.[5–9] As an abundant, renewable, and inexpensive C1 resource, converting inert CO_2 into reactive CO is a key process for reuse after its capture. The CO or syngas produced from this process can be coupled with Fischer–Tropsch synthesis or carbonylation reactions to convert CO_2 [10,11] into hydrocarbon liquid fuels or high-value chemicals such as aldehydes, alcohols, carboxylic acids and esters,[2,9,12,13] thereby realizing the carbon cycling. Therefore, developing key technologies for CO_2 conversion has attracted extensive research.

The reverse water gas shift (RWGS) reaction is an effective means of converting CO_2 into CO ($CO_2 + H_2 \rightarrow CO + H_2O$, $\Delta H_{298K} = 41.1$ kJ mol^{-1}).[14,15] This reaction skillfully circumvents the complex technical challenges and high energy costs associated with the direct conversion of CO_2 into liquid hydrocarbons, demonstrating significant potential in the field of carbon recycling. Advances in the RWGS process have focused on

improving catalyst efficiency, reducing energy consumption, especially the exploration of new catalytic materials and reaction conditions that enhance CO selectivity and conversion rates.[16,17]

Transition metal carbides (TMCs) are a class of materials with unique electronic structures and noble-metal-like properties.[18–20] They are inexpensive and abundant, and have been widely studied as promising alternative catalysts for noble metal catalysts or supports.[21,22] Molybdenum carbide (MoC), as a typical representative of TMC catalysts, has shown good performance in RWGS reaction, including high activity, selectivity towards CO, and resistance to coking.[23–29] Especially, MoC catalysts can operate effectively at lower temperatures than traditional metal-based catalysts, while maintaining good stability.[24] The inherent properties of MoC, such as its ability to activate CO_2 and H_2, make it a promising candidate for RWGS applications.

MoC exists in various crystalline structures,[30] including hexagonal and cubic forms, each exhibiting distinct catalytic behaviors in the RWGS reaction. The face-centered cubic α-MoC catalyst (also known as δ-MoC in some literature) exhibits excellent water dissociation capabilities, producing numerous hydroxyl groups on its surface during the reaction. Metals loaded on the α-MoC support can be highly dispersed or form stable single-atom catalysts through strong interactions with the support, creating new active sites at the interface. Consequently, high reaction activity for the WGS/RWGS reaction can be observed even at low temperatures.[23–26] For hexagonal phase, Wang *et al.*[31] calculated the adsorption of hydrogen on different

surfaces of hexagonal phase Mo_2C under various coverages using density functional theory (DFT) and found that the dissociative adsorption of H_2 on the Mo termination of (001) and (100) surfaces, as well as Mo/C mixed termination of (101) and (201) surfaces, is kinetically and thermodynamically favorable. The results show that MoC has excellent ability to activate H_2. Zhang et al.[32] synthesized $Cu/\beta-Mo_2C$ catalysts by using $\beta-Mo_2C$ as support, which significantly promoted the uniform dispersion of Cu on the surface of $\beta-Mo_2C$ and avoided the deactivation of the catalysts due to sintering at high temperatures, thus exhibiting high RWGS catalytic activity and excellent stability. Galallah et al.[33] prepared Mo_2C@CN using carbon–nitride (CN) as the support, achieving a CO_2 conversion rate of approximately 76% at 700 °C, with high CO selectivity (87%) and very low CH_4 selectivity (2%). The addition of potassium as a promoter further improved the selectivity for CO to 99%. This outcome exemplifies the remarkable RWGS reaction activity.

γ-MoC, similar to $\beta-Mo_2C$, is a hexagonal-phase MoC[34] and its crystal surfaces exhibit typical metallic properties, resulting in high electrocatalytic performance. It shows outstanding hydrogen evolution reaction (HER) and oxygen evolution reaction (OER)[35–39] activity. Compared to the extensive research on its electrochemical activity, there is little research on its RWGS activity or other thermal catalytic reaction, partly due to the poor thermal stability of this phase at high temperatures. In 2014, γ-MoC was successfully prepared as a stable pure nanomaterial for the first time.[36] Further exploration of the RWGS reaction activity on this γ-MoC therefore has become valuable. This work aims to study the RWGS reaction mechanism on γ-MoC through DFT calculations, and the Mo-terminated γ-MoC(100) surface was used as the model. Based on the DFT results, the RWGS activity of γ-MoC is further compared with α-MoC, MoP and metallic Mo.

2 Computational methods and models

2.1 Calculation methods

All calculations in this work were performed using the DS-PAW package which is based on the projector augmented wave (PAW) pseudopotential.[40] The Perdew–Burke–Ernzerhof (PBE) functional with the generalized gradient approximation (GGA) was adopted.[41] The plane-wave cutoff energy was set to 400 eV. For structure relaxation, the force tolerance and energy difference were respectively set to lower than 0.02 eV Å^{-1} and 10^{-4} eV. All the energies in this work included zero-point energy (ZPE) correction. Transition state calculations were done using the NEB method within DS-PAW.

The adsorption energy E_{ads} of species on the catalyst surface is defined as:

$$E_{ads} = E_{(x/slab)} - E_{(x)} - E_{(slab)}$$

where $E_{(x/slab)}$ represents the total energy of species x adsorbed on the catalyst surface, $E_{(x)}$ is the energy of species x in the gas phase, and $E_{(slab)}$ is the energy of the clean surface.
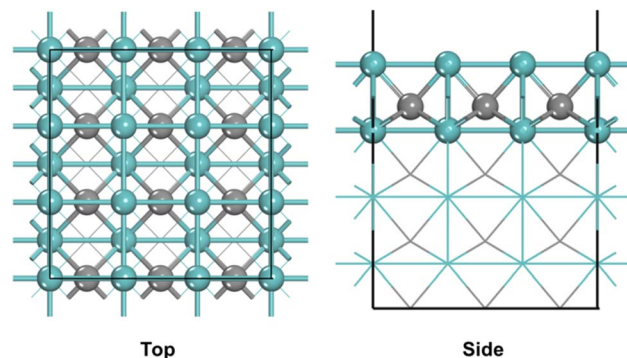

Fig. 1   Top and side views of the γ-MoC(100) surface (blue and gray balls represent Mo and C atoms, respectively).

2.2 Model

A WC-type γ-MoC was chosen and the bulk parameters after optimized were found to be $a = b = 2.93$ Å and $c = 2.84$ Å, which were in good agreement with experimental results.[42,43] The Mo-terminated (100) surface that has only Mo atoms exposed was selected. A $p(3 \times 3)$ supercell with eight atomic layers was used as the model (Fig. 1), and the bottom four layers of the model are fixed, and the top four layers are allowed to relax. In order to avoid strong interactions between the layers, the vacuum layer was set to 15 Å. The Brillouin zone was sampled by Monkhorst–Pack scheme using $3 \times 3 \times 1$ k-points grids.

3 Results and discussion

3.1 Adsorption of RWGS intermediates on γ-MoC(100) surface

The RWGS reaction may commonly follow four primary mechanisms.[28,29] Among them, the carbonate mechanism is generally more favorable on oxide catalyst surfaces, particularly on basic oxides and transition metal oxides.[28,29,44–48] Due to the nature of MoC catalyst surface, surface O can only be obtained from dissociation of CO_2, and the combination of CO_2 and O is endothermic by at least 1.61 eV (Fig. S1†). The energy is considerably high. Therefore, detailed carbonate mechanism was not considered in this work, and only the other three mechanisms were discussed in the following. As shown in Table 1, the first one is the redox mechanism, also known as the direct dissociation mechanism, where CO_2* directly dissociates into CO* and O* species (R2), H_2 does not directly participate in CO_2 reduction, just reduces the surface O* atom to form H_2O* (R10 and R11). The second one is carboxy mechanism, which dissociated H* reacts firstly with CO_2* to form COOH* intermediate (R3), and then COOH* undergoes one or two step decomposition reactions to generate CO* (R4–R6). The third one is formate mechanism, which dissociated H* reacts firstly with CO_2* to form HCOO* intermediate (R7), and then HCOO* undergoes two step decomposition reactions to generate CO* (R8 and R9).

As shown in Table 1, 10 main intermediates, including CO_2, H_2, CO, H_2O, C, H, O, OH, COOH and HCOO are involved in

Table 1 The elementary steps involved in the RWGS mechanisms (* denotes the catalyst active site or the surface-adsorbed species)

Mechanism	Label	Elementary reaction
Redox mechanism	R0	$CO_2^* + ^* \rightarrow CO_2^*$
	R1	$H_2 + 2^* \rightarrow H^* + H^*$
	R2	$CO_2^* + ^* \rightarrow CO^* + O^*$
	R10	$O^* + H^* \rightarrow OH^* + ^*$
	R11	$OH^* + H^* \rightarrow H_2O^* + ^*$
Carboxy mechanism	R0	$CO_2 + ^* \rightarrow CO_2^*$
	R1	$H_2 + 2^* \rightarrow H^* + H^*$
	R3	$CO_2^* + H^* \rightarrow COOH^* + ^*$
	R4	$COOH^* + ^* \rightarrow CO^* + OH^*$
	R5	$COOH^* + ^* \rightarrow COH^* + O^*$
	R6	$COH^* + ^* \rightarrow CO^* + H^*$
	R10	$O^* + H^* \rightarrow OH^* + ^*$
	R11	$OH^* + H^* \rightarrow H_2O^* + ^*$
Formate mechanism	R0	$CO_2 + ^* \rightarrow CO_2^*$
	R1	$H_2 + 2^* \rightarrow H^* + H^*$
	R7	$CO_2^* + H^* \rightarrow HCOO^* + ^*$
	R8	$HCOO^* + ^* \rightarrow CHO^* + O^*$
	R9	$CHO^* + ^* \rightarrow CO^* + H^*$
	R10	$O^* + H^* \rightarrow OH^* + ^*$
	R11	$OH^* + H^* \rightarrow H_2O^* + ^*$

Table 2 The most stable adsorption site and the adsorption energy (E_{ads}, eV) of each intermediate on the γ-MoC(100) surface

Species	γ-MoC(100)	
	Site	E_{ads}
C	Hollow	−10.33
H	Bridge	−0.74
O	Hollow	−4.50
CO_2	Hollow	−2.14
H_2	Top	−0.51
CO	Hollow	−3.06
H_2O	Bridge	−0.84
OH	Hollow	−5.05
COOH	Hollow	−4.29
HCOO	Hollow	−5.47

vertically at the hollow site, with O interacting with the 4 surrounding surface Mo atoms. Both COOH and HCOO adsorb at the hollow sites and interact with the surface through both C and O atoms. For the convenience of comparison with future experimental infrared spectral data, the calculated vibration frequencies of different intermediates are afforded (Table S1†).

these three mechanisms. We first studied the adsorption of these intermediates on the γ-MoC(100) surface. The configurations of these intermediates at the most stable adsorption site are shown in Fig. 2. Table 2 lists the adsorption energy and the corresponding adsorption site of each intermediate.

As shown in Fig. 2, on the γ-MoC(100) surface, CO_2 and CO preferentially adsorb at the hollow sites, interacting with the surrounding Mo atoms through their C and O atoms, and in the chemisorbed state, CO_2 is transformed from a linear to a bent structure. H_2 molecule stably adsorbs parallel to the surface at the Mo top site, while H_2O stably adsorbs at the Mo–Mo bridge site. The most stable adsorption sites for C and O are the hollow sites, whereas H species locates at the bridge site. OH adsorbs

3.2 RWGS reaction mechanism on γ-MoC(100) surface

The reaction begins with the adsorption of CO_2 and H_2 on the catalyst surface. CO_2 adsorbs at the hollow site formed by four surface Mo atoms with $E_{ads} = −2.14$ eV, while H_2 adsorbs at the Mo top site with $E_{ads} = −0.51$ eV. Subsequently, H_2^* undergoes dissociation (R1), with the dissociation energy barrier of only 0.08 eV (Table 3) and the process is exothermic by 0.87 eV. Therefore, we deduce that the H_2 molecule is very easy to dissociate and surface H* is abundant. Our previous studies of RWGS on Mo and MoP catalysts[49,50] suggested redox mechanism is more preferable, therefore, we calculated mainly redox mechanism on the γ-MoC(100) surface while considering the possibility of CO_2 direct hydrogenation into COOH* or HCOO*,
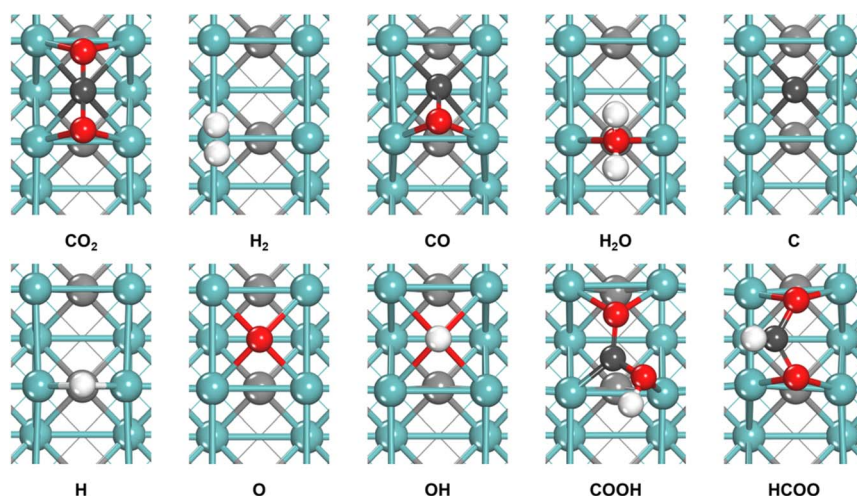

Fig. 2 The most stable adsorption configurations of intermediates on the γ-MoC(100) surface (blue, red, white and gray balls represent Mo, O, H and bulk-C atoms, respectively. To distinguish the C atoms in the adsorbate, they are represented in black balls).

Table 3 Energy barriers (E_a, eV), reaction energies (E_r, eV) and bond lengths (d, Å) of transition states in RWGS reaction on the γ-MoC(100) surface

| | | γ-MoC(100) | | |
Label	Elementary reaction	E_a	E_r	d
R1	$H_2^* \rightarrow H^* + H^*$	0.08	−0.87	1.173
R2	$CO_2^* \rightarrow CO^* + O^*$	0.83	−2.04	1.866
R3	$CO_2^* + H^* \rightarrow COOH^*$	1.66	1.19	1.352
R7	$CO_2^* + H^* \rightarrow HCOO^*$	0.62	0.27	1.673
R8	$HCOO^* \rightarrow CHO^* + O^*$	1.13	−1.59	1.919
R10	$O^* + H^* \rightarrow OH^*$	2.15	1.52	1.239
R11	$OH^* + H^* \rightarrow H_2O^*$	1.48	1.33	1.244
R12	$OH^* + OH^* \rightarrow H_2O^* + O^*$	0.06	0.15	1.257/1.168

i.e. the initial steps of the carboxy and formate mechanisms. The potential energy surface based on the calculation results is shown in Fig. 3. The initial states (IS), transition states (TS) and final states (FS) of the RWGS elementary steps on the γ-MoC(100) surface are shown in Fig. 4.

In the redox pathway, CO_2 initially adsorbs at the hollow site as the IS2, as shown in Fig. 4. After passing through the transition state TS2, one of the C–O bonds is broken, forming co-adsorbed CO^* and O^* on the surface with the dissociation energy barrier of 0.83 eV. Subsequently, the hydrogenation process of O^* to form OH^* has a high barrier of 2.15 eV, and is endothermic by 1.52 eV, indicating that the formation of OH^* is relatively difficult. The reaction energy barrier for the further hydrogenation of OH^* to form H_2O^* is 1.48 eV, and the reaction is endothermic by 1.33 eV. Notably, H_2O^* can also be obtained by the disproportionation of OH^* ($2OH^* \rightarrow H_2O^* + O^*$), with the barrier significantly reduced to 0.06 eV. The results prove that H_2O^* formation is more likely through the disproportion-ation pathway.

In contrast, through the carboxy mechanism pathway, the energy barrier of CO_2^* hydrogenation to form $COOH^*$ is 1.66 eV, and the reaction is endothermic with $E_r = 1.19$ eV. The barrier is considerably higher than that of redox pathway. However, through the formate mechanism pathway, the H^* interacts with the C atom of CO_2^* to form $HCOO^*$ species, with a barrier of only 0.62 eV, which is still lower than that of CO_2^* direct

dissociation (0.83 eV). Although this step is kinetically advantageous, it is endothermic by 0.27 eV, which is thermodynamically unfavored compared to the strongly exothermic process of CO_2^* direct dissociation. Furthermore, the further dissociation of $HCOO^*$ needs to overcome a barrier of 1.13 eV, which makes the formate mechanism more difficult. Interestingly, Bader charge analysis showed that, the charge of C and O atom in CO_2^* is +0.49e and −1.05e, respectively. The charge of surface H is −0.46e. As the configuration of CO_2 is transformed from a linear to a bent structure in the chemisorbed state, its HUMO and LUMO orbitals also changed correspondingly. As shown in Fig. S2,† the HUMO orbital is mainly contributed by O atoms while the LUMO orbital is mainly contributed by C atom. Therefore, the negatively charged surface H can easily interact with the LUMO orbital of bent CO_2, that is, H attacks C to undergo nucleophilic reactions and generate $HCOO^*$. On the contrary, it is very difficult for surface H to attack O, which is also negatively charged, and interact with the LUMO orbital of bent CO_2. This also explains why CO_2^* hydrogenation into $COOH^*$ has much higher barrier than into the $HCOO^*$ species. Just as shown in Fig. 3, the redox pathway is more favorable than the other two pathways, and may be the mechanism with the greatest contribution of RWGS reaction on γ-MoC(100) surface. Considering the whole reaction process, it is found that the CO desorption from the surface requires a substantial energy of 3.06 eV. The huge energy gap made this desorption very difficult, and it is rational to deduce that the further dissociation or hydrogenation of CO^* is much possible. We suppose that with the RWGS reaction, CO_2 can be directly used as a substitute carbon source for CO on the γ-MoC(100) surface for further reaction, without firstly generating CO and then cascade other reactions.

3.3 Comparison of γ-MoC and other Mo-based catalysts

We have previously investigated the RWGS reaction mechanism on the Mo(100) and MoP(100) surfaces.[49,50] Comparing the results on these three surfaces (Fig. 5), it can be seen that the adsorption energies of CO_2 on the γ-MoC(100) and Mo(100) surfaces are higher than that on the MoP(100) surface. The order of adsorption energy is: MoP(100) (−1.20 eV) < γ-MoC(100) (−2.14 eV) < Mo(100) (−2.54 eV). The dissociation energy barriers of CO_2^* on these three surfaces follow the order: MoP(100) (0.47 eV) < Mo(100) (0.67 eV) < γ-MoC(100) (0.83 eV). The barriers of OH^* formation on the Mo(100) and MoP(100) surfaces were also listed for comparison due to the high value of that on the γ-MoC(100) surface. It is found that the OH^* formation barrier is very close on the Mo(100) and MoP(100) surfaces (1.23 *vs.* 1.18 eV), and much lower than that on the γ-MoC(100) surface (2.15 eV). Interestingly, the desorption of CO on the Mo(100) surface is also very high (3.22 eV) just like on the γ-MoC(100) surface (3.06 eV), while it is lower on the MoP(100) surface (2.07 eV). In contrast, H_2O desorption is much easier on all three surfaces. The desorption energies are 0.91, 0.58 and 0.84 eV, respectively.

It is noted that MoP and γ-MoC are both WC-type and have very similar crystal structure, and they have the same Mo : P/
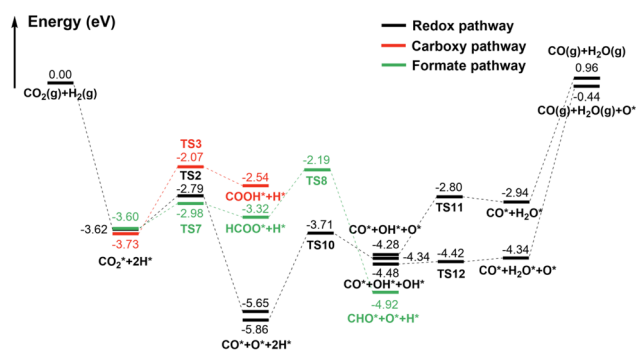

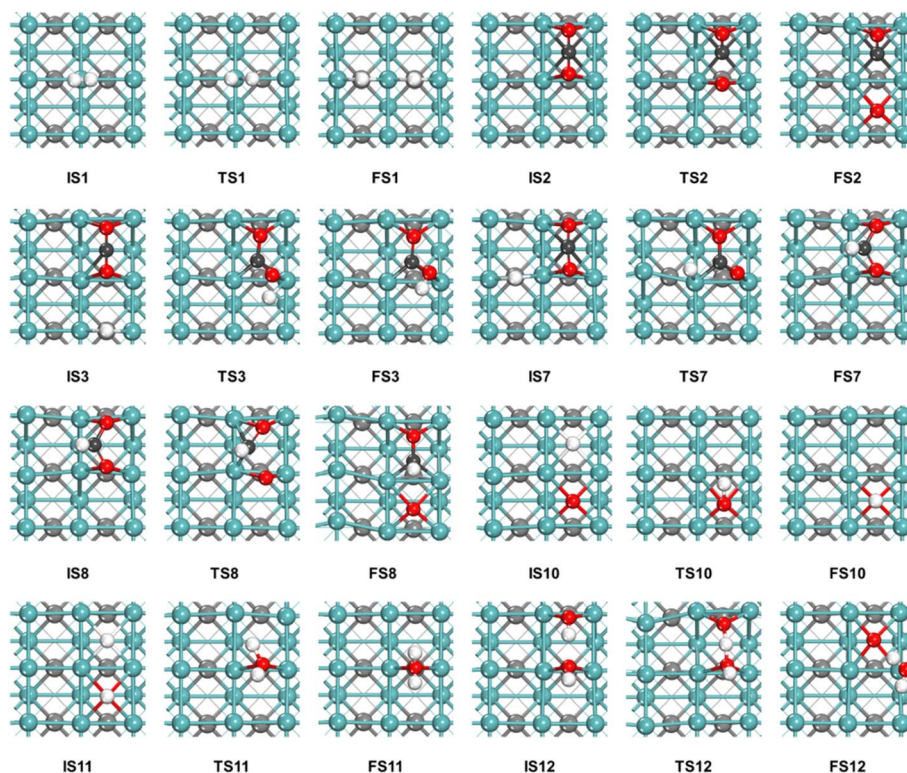**Fig. 3** The potential energy surface of RWGS reaction on the γ-MoC(100) surface.

Fig. 4   The initial states (IS), transition states (TS) and final states (FS) of the RWGS elementary steps on the γ-MoC(100) surface.
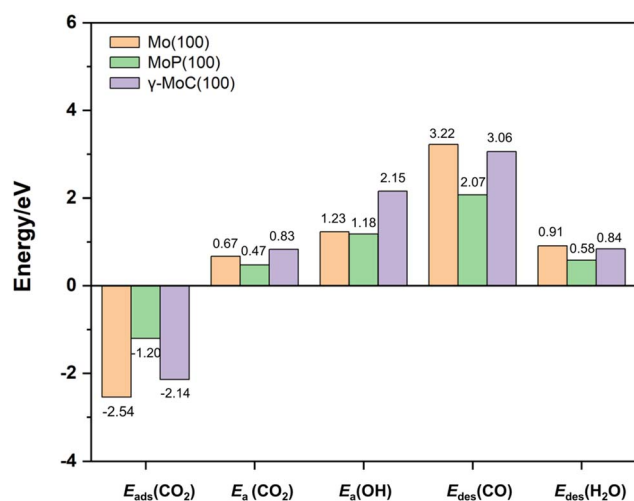

Fig. 5   The adsorption energies (E_{ads}, eV) of CO_2, energy barriers (E_a, eV) of CO_2* dissociation, energy barriers of OH* formation and the desorption energies (E_{ads}, eV) of CO_2 and CO on the (100) surfaces of different catalysts.

Mo : C stoichiometric ratio (1 : 1). Bader charge analysis showed that, the charge transfer from Mo to P in bulk MoP is 0.74e, while from Mo to C in bulk γ-MoC is 1.25e. We suppose that the charge transfer leads to the weaker adsorption of CO_2 on MoP(100) and γ-MoC(100) surfaces when compared to the Mo(100). And the significant differences of CO_2 adsorption energy on MoP(100) and γ-MoC(100) surfaces may be due to

their different adsorption sites. Unlike the 4-fold hollow site adsorption on the γ-MoC(100) surface, CO_2 is adsorbed at a bridge site on the MoP(100) surface, interacting only with two surface Mo atoms.

Overall, MoP(100) surface has moderate CO_2, CO and H_2O adsorption energies, as well as the lowest CO_2* dissociation barrier and OH* formation barrier. From the perspective of RWGS reaction efficiency, MoP(100) should be the best among the three surfaces.

Lin et al.[23] investigated the WGS reaction mechanism on Pt/α-MoC catalysts under low-temperature conditions. They modeled the Mo termination of α-MoC(111) surface based on experimental characterization results. Using their data, we deduced the RWGS reaction pathway (the energy difference caused by calculation method was ignored). For the convenience of comparison, the potential energy surfaces of the redox mechanism of RWGS reaction on the γ-MoC(100) and α-MoC(111) surfaces are shown in Fig. 6. It can be found that, the adsorption energy of CO_2 on the α-MoC(111) surface (−1.44 eV) is lower than that on the γ-MoC(100) surface (−2.14 eV). According to the projected density of states (PDOS) of the two surfaces (Fig. S3†), near the Fermi level, the total electron density and Mo orbital density of the γ-MoC(100) surface are higher than those of α-MoC(111) surface, indicating the stronger interaction with CO_2. Furthermore, CO_2* has lower dissociation barrier on the α-MoC(111) surface (0.45 eV) than that on the γ-MoC(100) surface (0.83 eV). The moderate adsorption energy of CO_2 and lower energy barrier of CO_2 dissociation result in more effective redox of CO_2 on the α-MoC(111) surface. In addition, the CO desorption is also easier
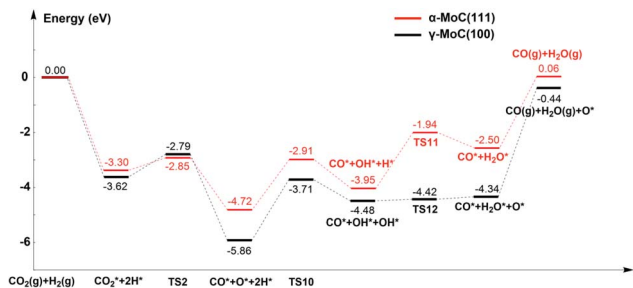
Fig. 6 The potential energy surfaces of RWGS reaction on the γ-MoC(100) and α-MoC(111) surfaces.

on the α-MoC(111) surface (2.28 eV or 1.62 eV when considering 4H co-adsorption). However, the H_2O^* formation barrier on the α-MoC(111) surface is much higher than that on the γ-MoC(100) surface (2.01 vs. 1.48/0.06 eV). We speculate that the disproportionation of OH* may also lower this energy barrier, but we do not have corresponding data. If that's the case, the whole RWGS efficiency on α-MoC(111) is also higher than that on γ-MoC(100), especially due to the easy desorption of CO (1.62/2.28 vs. 3.06 eV).

4 Conclusion

The RWGS reaction mechanism on the γ-MoC(100) surface has been investigated using DFT. CO_2 has a strong interaction with the γ-MoC(100) surface, and the adsorption energy is 2.14 eV. The redox mechanism is found to be the most preferred pathway. CO_2^* directly dissociated into CO* and O*, with a moderate barrier (0.83 eV), and the formation of OH* has high barrier of 2.15 eV. OH* further hydrogenates into H_2O^* has a barrier of 1.48 eV. However, the disproportionation of OH* considerably lower this value to 0.06 eV. Interestingly, the most difficult step is the desorption of CO due to the large energy demand of 3.06 eV. CO* may tend to undergo further hydrogenation or direct dissociation on the surface instead. Although the RWGS performance of γ-MoC(100) surface is not as good as other Mo-based catalysts, it has a relative low energy barrier for activating CO_2, and the strong binding energy of CO to the surface is actually beneficial for further carbon conversion reactions. This offers a unique opportunity for CO_2 to serve as an alternative carbon source for CO, bypassing the traditional need to first convert CO_2 into CO before proceeding with subsequent reactions.

Data availability

Structure files, supported figures and tables used in this article have been included as part of the ESI.†

Author contributions

Xiaoshu Yao: conceptualization, investigation, data curation, software, visualization, writing – original draft. Jingyuan Mei and Xianhui Guo: investigation, formal analysis. Zhihong Wei: conceptualization, formal analysis, funding acquisition,

supervision. Xinxin Tian: conceptualization, methodology, funding acquisition, supervision, resources, writing – review & editing.

Conflicts of interest

There are no conflicts to declare.

Acknowledgements

References

1 Y. Ou, C. Roney, J. Alsalam, K. Calvin, J. Creason, J. Edmonds, A. A. Fawcett, P. Kyle, K. Narayan, P. O'Rourke, P. Patel, S. Ragnauth, S. J. Smith and H. McJeon, *Nat. Commun.*, 2021, **12**, 6245–6253.

2 Z. Zhang, S. Y. Pan, H. Li, J. C. Cai, A. G. Olabi, E. J. Anthony and V. Manovic, *Renewable Sustainable Energy Rev.*, 2020, **125**, 109799–109815.

3 S. Davoodi, M. Al-Shargabi, D. A. Wood, V. S. Rukavishnikov and K. M. Minaev, *J. Nat. Gas Sci. Eng.*, 2023, **117**, 205070–205097.

4 J. Yao, H. Han, Y. Yang, Y. Song and G. Li, *Appl. Sci.*, 2023, **13**, 1169–1195.

5 S. Yuan, D. Ma, J. Li, T. Zhou, Z. Ji and H. Han, *Adv. Pet. Explor. Dev.*, 2022, **49**, 955–962.

6 K. Jiang, P. Ashworth, S. Zhang, X. Liang, Y. Sun and D. Angus, *Renewable Sustainable Energy Rev.*, 2020, **119**, 109601–109615.

7 J. F. D. Tapia, J. Y. Lee, R. E. H. Ooi, D. C. Y. Foo and R. R. Tan, *Sustain. Prod. Consum.*, 2018, **13**, 1–15.

8 B. Dziejarski, R. Krzyżyńska and K. Andersson, *Fuel*, 2023, **342**, 127776–127813.

9 T. A. Saleh, *RSC Adv.*, 2022, **12**, 23869–23888.

10 J. Ren, J. P. Cao, X. Y. Zhao, F. L. Yang and X. Y. Wei, *Renewable Sustainable Energy Rev.*, 2019, **116**, 109426–109450.

11 J. Ren, Y. L. Liu, X. Y. Zhao and J. P. Cao, *J. Energy Inst.*, 2020, **93**, 1083–1098.

12 T. A. Saleh, *Bull. Mater. Sci.*, 2022, **45**, 101413–101434.

13 Y. He, F. H. Müller, R. Palkovits, F. Zeng and C. Mebrahtu, *Appl. Catal., B*, 2024, **345**, 123663–123693.

14 A. M. Bahmanpour, M. Signorile and O. Kröcher, *Appl. Catal., B*, 2021, **295**, 120319–120329.

15 Y. A. Daza and J. N. Kuhn, *RSC Adv.*, 2016, **6**, 49675–49691.

16 X. Zhang, Y. Liu, M. Zhang, T. Yu, B. Chen, Y. Xu, M. Crocker, X. Zhu, Y. Zhu, R. Wang, D. Xiao, M. Bi, D. Ma and C. Shi, *Chem*, 2020, **6**, 3312–3328.

17 A. Saravanan, P. S. Kumar, D. V. N. Vo, S. Jeevanantham, V. Bhuvaneswari, V. A. Narayanan, P. R. Yaashikaa,

S. Swetha and B. Reshma, *Chem. Eng. Sci.*, 2021, **236**, 116515–116530.

18 P. Chen, J. Ye, H. Wang, L. Ouyang and M. Zhu, *J. Alloys Compd.*, 2021, **883**, 160833–160853.

19 Q. Gao, W. Zhang, Z. Shi, L. Yang and Y. Tang, *Adv. Mater.*, 2018, **31**, 1802880.

20 D. Tian, S. R. Denny, K. Li, H. Wang, S. Kattel and J. G. Chen, *Chem. Soc. Rev.*, 2021, **50**, 12338–12376.

21 H. Prats and M. Stamatakis, *J. Phys. Chem. Lett.*, 2024, **15**, 3450–3460.

22 H. Prats and M. Stamatakis, *J. Mater. Chem. A*, 2022, **10**, 1522–1534.

23 L. Lin, W. Zhou, R. Gao, S. Yao, X. Zhang, W. Xu, S. Zheng, Z. Jiang, Q. Yu, Y. W. Li, C. Shi, X. D. Wen and D. Ma, *Nature*, 2017, **544**, 80–83.

24 S. Y. Yao, X. Zhang, W. Zhou, R. Gao, W. Q. Xu, Y. F. Ye, L. L. Lin, X. D. Wen, P. Liu, B. B. Chen, E. Crumlin, J. H. Guo, Z. J. Zuo, W. Z. Li, J. L. Xie, L. Lu, C. J. Kiely, L. Gu, C. Shi, J. A. Rodriguez and D. Ma, *Science*, 2017, **357**, 389–393.

25 L. Sun, J. Xu, X. Liu, B. Qiao, L. Li, Y. Ren, Q. Wan, J. Lin, S. Lin, X. Wang, H. Guo and T. Zhang, *ACS Catal.*, 2021, **11**, 5942–5950.

26 J. Li, L. Sun, Q. Wan, J. Lin, S. Lin and X. Wang, *J. Phys. Chem. Lett.*, 2021, **12**, 11415–11421.

27 Q. Zhang, L. Pastor-Pérez, S. Gu and T. Ramirez Reina, *Catalysts*, 2020, **10**, 955–975.

28 X. Su, X. Yang, B. Zhao and Y. Huang, *J. Energy Chem.*, 2017, **26**, 854–867.

29 M. González-Castaño, B. Dorneanu and H. Arellano-García, *React. Chem. Eng.*, 2021, **6**, 954–976.

30 C. Chu, C. Li, X. Liu, H. Zhao, C. Wu, J. Li, K. Liu, Q. Li and D. Cao, *Catal. Sci. Technol.*, 2022, **12**, 1130–1143.

31 T. Wang, Y. W. Li, J. Wang, M. Beller and H. J. Jiao, *J. Phys. Chem. C*, 2014, **118**, 8079–8089.

32 X. Zhang, X. Zhu, L. Lin, S. Yao, M. Zhang, X. Liu, X. Wang, Y. W. Li, C. Shi and D. Ma, *ACS Catal.*, 2016, **7**, 912–918.

33 A. G. Galallah, M. K. Albolkany, A. E. Rashed, W. Sadik, A. G. El-Demerdash and A. A. El-Moneim, *J. Environ. Chem. Eng.*, 2024, **12**, 113380–113391.

34 J. Lu, H. Hugosson, O. Eriksson, L. NordstroÈm and U. Jansson, *Thin Solid Films*, 2000, **370**, 203–212.

35 X. Zhang, L. Huang, Y. Han, M. Xu and S. Dong, *Nanoscale*, 2017, **9**, 5583–5588.

36 C. Wan, Y. N. Regmi and B. M. Leonard, *Angew. Chem., Int. Ed.*, 2014, **53**, 6407–6410.

37 Y. Cheng, J. Gong, B. Cao, X. Xu, P. Jing, B. Liu, R. Gao and J. Zhang, *ACS Catal.*, 2021, **11**, 3958–3974.

38 T. T. Yang and W. A. Saidi, *J. Phys. Chem. Lett.*, 2020, **11**, 2759–2764.

39 G. Q. Yu, W. J. Yin and X. B. Li, *Int. J. Hydrogen Energy*, 2022, **47**, 13664–13673.

40 P. E. Blöchl, *Phys. Rev. B:Condens. Matter Mater. Phys.*, 1994, **50**, 17953–17979.

41 J. P. Perdew, K. Burke and M. Ernzerhof, *Phys. Rev. Lett.*, 1996, **77**, 3865–3868.

42 A. Chrysanthou and P. Grieveson, *J. Mater. Sci. Lett.*, 1991, **10**, 145–146.

43 H. W. Hugosson, O. Eriksson, L. Nordström, U. Jansson, L. Fast, A. Delin, J. M. Wills and B. Johansson, *J. Appl. Phys.*, 1999, **86**, 3758–3767.

44 D. Ferri, T. Bürgi and A. Baiker, *Phys. Chem. Chem. Phys.*, 2002, **4**, 2667–2672.

45 A. Gogue, F. C. Meunier, D. Tibiletti, J. P. Breen and R. Burch, *J. Phys. Chem. B*, 2004, **108**, 20240–20246.

46 P. Panagiotopoulou, D. I. Kondarides and X. E. Verykios, *J. Phys. Chem. C*, 2011, **115**, 1220–1230.

47 L. L. Zhou, S. Q. Li, C. Ma, X. P. Fu, Y. S. Xu, W. W. Wang, H. Dong, C. J. Jia, F. R. Wang and C. H. Yan, *J. Am. Chem. Soc.*, 2023, **145**, 2252–2263.

48 M. A. Khoshooei, X. Wang, G. Vitale, F. Formalik, K. O. Kirlikovali, R. Q. Snurr, P. Pereira-Almao and O. K. Farha1, *Science*, 2024, **384**, 540–546.

49 Q. S. Lei, *DFT Study on the Mechanism of Reverse Water Gas Shift Reaction on Metallic Mo Surface*, Undergraduate thesis, Shanxi University, 2022.

50 X. S. Yao, *The Mechanism Study of Reverse Water Gas Shift Reaction on Mo-Based Catalyst*, Master Thesis, Shanxi University, 2024.